Impact of partial coherence on the apparent optical transfer function derived from the response to amplitude edges

Shakeri, S. Mojtaba; Van Vliet, Lucas J.; Stallinga, Sjoerd

DOI
10.1364/AO.56.003518

Publication date
2017

Document Version
Accepted author manuscript

Published in
Applied Optics

The impact of partial coherence on the apparent optical transfer function derived from the response to amplitude edges

S. Mojtaba Shakeri, Lucas J. van Vliet, and Sjoerd Stallinga*

Department of Imaging Physics, Delft University of Technology, Lorentzweg 1, 2628 CJ, Delft, The Netherlands
*Corresponding author: s.stallinga@tudelft.nl

Ocis-codes: (110.4980) Partial coherence in imaging; (110.4500) Optical transfer functions; (170.0180) Microscopy; (110.2990) Image formation theory.

Published as: S.M. Shakeri, L.J. van Vliet and S. Stallinga, 'Impact of partial coherence on the apparent optical transfer function derived from the response to amplitude edges', Applied Optics, 56, pp. 3518-3530, 2017. Available at publisher's website: https://www.osapublishing.org/ao/abstract.cfm?uri=ao-56-12-3518

Abstract: We present an investigation of the impact of partial coherence on optical imaging systems with the focus on Whole Slide Imaging (WSI) systems for digital pathology. The investigation is based on the analysis of the edge response of the optical system, which gives rise to an apparent Optical Transfer Function (OTF) that can be linked to two elementary complex functions Q and U. The function Q is directly related to the Transmission Cross-Coefficient (TCC) and can be identified with the performance function first introduced by Kintner and Stillitto. The function U depends on the TCC in a more involved way. When there are no aberrations the Q-function corresponds to the real part of the apparent OTF and the U function to the imaginary part of the apparent OTF. Close to the incoherent limit the effect of the U function is a mere shift of the edge compared to the fully incoherent case. We propose a new expression for the dependence of the Depth Of Focus (DOF) on spatial frequency and on the partial coherence factor σ, and validate it by simulation. Partial coherence effects are investigated experimentally on a WSI-system with a compact LED-based Köhler illumination unit with variable condenser NA. This unit incorporates a top hat diffuser for providing a reasonably uniform illumination field, with variations below 10% across the imaged Field Of View (FOV). The measurements of the apparent through-focus OTF derived from edges on a custom resolution chart for different σ were substantially in agreement with the simulations. Finding an optimal value for σ is not straightforward as lateral resolution and the level of edge ringing improve with increasing σ, whereas edge contrast and DOF improve with decreasing σ. We assess that the

tradeoff for the particular application of WSI systems for digital pathology is optimized for a σ value in the range of 0.55 to 0.75.

1 Introduction

Partial coherence influences image formation in microscopy via the partial coherence factor $\sigma = \mathrm{NA_{ill}}/\mathrm{NA}$, the ratio between the illumination (condenser) Numerical Aperture $\mathrm{NA_{ill}}$ and the imaging (objective) NA [1, 2, 3]. The imaging system transmits spatial frequencies of the sample up to the cutoff $(1+\sigma)\mathrm{NA}/\lambda$ (with λ the wavelength), so that the resolution increases towards the incoherent limit. On the other hand, the sharpness in the image, that can be quantified by the steepness of the edge response, improves towards the coherent limit. This beneficial effect, however, is accompanied by edge ringing artefacts. A trade-off between these effects can subjectively be defined based on the imaging application that is considered. A general rule of thumb in the field of microscopy is to slightly sacrifice resolution for image sharpness by reducing the illumination $\mathrm{NA_{ill}}$ to about 0.75 times the imaging NA.

This partial coherence tradeoff becomes even more involved when aberrations are taken into account. Several theoretical studies have appeared with regard to this issue. Barakat [4] investigated the effect of defocus and coma on amplitude edge and bar objects under partially coherent illumination. He found that the edge in the image is shifted compared to the edge in the underlying object towards the bright side of the edge, where the shift increases with decreasing σ. This topic has received further attention by Kirk [5] in the context of linewidth measurements with a microscope. Ichioka and Suzuki [6] studied complex periodic objects, and Hild et al. [7] studied the behavior of the intensity distribution and its first derivative for amplitude, phase and amplitude/phase bars. They found that the asymmetric behavior of the first derivative is strongly correlated with σ and the phase content of the object.

In particular the sensitivity of the optical system with respect to defocus, quantified by the Depth Of Focus (DOF), is a highly relevant parameter. It appears that the DOF increases towards the coherent limit [8, 9], although no comprehensive study has appeared on this aspect. In the field of lithography, an optimum value for the imaging NA and σ is found based on a desired DOF and a particular mask pattern [10, 11], even introducing novel metrics for DOF [12]. Von Waldkirch et al. [13, 14] investigated the influence of partial coherence on the DOF for a retinal projection display. They showed that a value for σ between 0.35 and 0.5 provided the best DOF for text readability. Ren et al. [15] have empirically studied the effect of the condenser NA on cytogenetic imaging with a brightfield microscope and found an optimum value of the partial coherence factor in the range 0.6 to 0.7. These examples imply that the optimum in the partial coherence tradeoff apparently depends on the application requirements.

Previously, we proposed a method for testing and monitoring the optical quality of Whole Slide Imaging (WSI) systems using a measurement of the through-focus Optical Transfer Function (OTF) obtained from the edge response

of a custom made resolution target [16]. In this analysis it was assumed that the imaging system is incoherent. As a partially coherent system is non-linear the OTF derived from the edge response is not a true transfer function but rather an apparent OTF. It may be expected, however, that it is still possible to use it to characterize the optical quality of the imaging system. Wernick and Morris [17] have analyzed the effects of partial coherence on the apparent MTF for square apertures, and found an increase in the apparent MTF for the lower spatial frequencies with decreasing σ. This reflects the increase in edge steepness towards the coherent limit. Kintner and Stillito [18] proposed to characterize the edge response of a partially coherent optical imaging systems by a single function, the so-called "performance function", for adequately describing the cross-over between the incoherent and coherent limits.

So far, an in-depth investigation of the apparent OTF derived from the edge response has not been reported. The impact of aberrations, in particular defocus, on the apparent OTF has also remained unclear. The goals of this paper are (i) to provide simulations and measurements of the effect of the partial coherence factor σ on the apparent OTF, (ii) assess effects of aberrations in the partial coherence regime, in particular the impact of defocus quantified by the DOF, (iii) evaluate the partial coherence tradeoff for the application in Whole Slide Imaging (WSI) systems for digital pathology.

This paper is structured as follows. In the theory and simulation section we first briefly summarize partial coherence theory, focusing on the apparent OTF derived from the edge response, and the effects of partial coherence on edge ringing, DOF, and the impact of aberrations. In the experiments section, we describe the design of a color sequential Köhler illumination unit used to measure the effect of the partial coherence factor on the apparent OTF. Finally, we will discuss the results and the implications for WSI systems.

2 Theory and simulation

2.1 Apparent transfer functions and performance function

According to Hopkins' treatment of partially coherent optical imaging systems [1, 2], the measured intensity on the detector is given by:

$$I(\vec{r}) = \int d^2r_1 d^2r_2 \, P(\vec{r}-\vec{r}_1) \, P^*(\vec{r}-\vec{r}_2) \, J(\vec{r}_1-\vec{r}_2) \, T(\vec{r}_1) \, T(\vec{r}_2)^* \qquad (1)$$

where $P(\vec{r})$ is the coherent Point Spread Function (PSF), $J(\vec{r})$ is the mutual intensity, $T(\vec{r})$ is the complex amplitude transmission of the object, and where $\vec{r}$, $\vec{r}_1$, and $\vec{r}_2$ are 2D position vectors. The integration domain is taken to extend from $-\infty$ to $+\infty$ for all integration variables. We adopt this convention in this paper unless the domain is specified explicitly. The Fourier Transform (FT) of the coherent PSF as a function of spatial frequency $\vec{q}$ is:

$$\hat{P}(\vec{q}) = C(\vec{q}\lambda/\mathrm{NA}) \exp\left(2\pi i W(\vec{q}\lambda/\mathrm{NA})/\lambda\right), \qquad (2)$$

where $W(\vec{\rho})$ is the aberration function, depending on the normalized pupil coordinates $\vec{\rho} = \vec{q}\lambda/\mathrm{NA}$, and where $C(\vec{\rho})$ is the circle function (equal to one inside the unit circle, equal to zero outside the unit circle). The FT of the mutual intensity is:

$$\hat{J}(\vec{q}) = \frac{1}{\pi a^2} C\left(\vec{q}\lambda/(\sigma \mathrm{NA})\right), \tag{3}$$

where $a = \min(\sigma, 1)$ and σ is the partial coherence factor. The intensity can be expressed in terms of the FT quantities as:

$$I(\vec{r}) = \int d^2q d^2q' \, S(\vec{q}, \vec{q}') \, \hat{T}(\vec{q}) \, \hat{T}(\vec{q}')^* \exp\left(2\pi i \left(\vec{q} - \vec{q}'\right) \cdot \vec{r}\right), \tag{4}$$

where $\vec{q}$ and $\vec{q}'$ are 2D spatial frequency vectors and where the so-called Transmission Cross Coefficient (TCC) is given by:

$$S(\vec{q}, \vec{q}') = \int d^2q'' \, \hat{J}(\vec{q}'') \, \hat{P}(\vec{q} + \vec{q}'') \, \hat{P}(\vec{q}' + \vec{q}'')^* . \tag{5}$$

The TCC can thus be evaluated from the overlap integral of the FT of the mutual intensity with two displaced pupil functions (see Fig. 1a). The FT of the mutual intensity is normalized such that $S(0,0) = 1$, implying that a uniform normalized object $T(\vec{r}) = 1$ gives rise to a uniform normalized intensity signal $I(\vec{r}) = 1$. It may be deduced that object spatial frequencies below $(1+\sigma)\,\mathrm{NA}/\lambda$ contribute to the intensity signal and that the highest spatial frequency in the intensity signal is $2\mathrm{NA}/\lambda$, regardless of the partial coherence factor σ. For $\sigma = 0$ we retrieve the fully coherent case, for $\sigma \to \infty$ we retrieve the fully incoherent case.

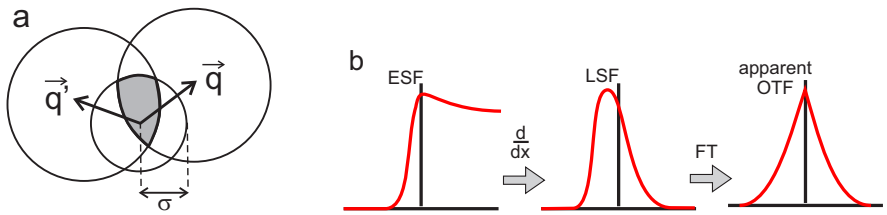

Figure 1: (a) Schematic illustration for evaluating the TCC according to Eq. (5) from the overlap integral of two displaced pupil functions with the FT of the mutual intensity. (b) Illustration of the steps to compute the apparent OTF from the measured amplitude edge response.

An important function in the subsequent analysis is:

$$\hat{Q}(\vec{q}) \equiv S(\vec{q}, 0) = \int d^2q' \, \hat{J}(\vec{q}') \, \hat{P}(\vec{q}')^* \, \hat{P}(\vec{q} + \vec{q}'), \tag{6}$$

Taking the inverse Fourier transform of this complex function gives:

$$Q(\vec{r}) = P(\vec{r}) \, \tilde{P}(\vec{r})^*, \tag{7}$$

where:

$$\tilde{P}\left(\vec{r}\right)=\int d^{2}q\,\hat{J}\left(\vec{q}\right)\hat{P}\left(\vec{q}\right)\exp\left(2\pi i\vec{q}\cdot\vec{r}\right). \tag{8}$$

The function $Q\left(\vec{r}\right)$ is called the performance function by Kintner and Stillitto [18]. For $\sigma\geq 1$ it reduces to the incoherent PSF, for $\sigma\ll 1$ it reduces to the coherent PSF. Sheppard arrives at (the FT of) the same function in the analysis of the response to weak objects in the context of quantitative phase imaging [19] and calls it the Weak OTF (WOTF).

We now apply this formalism to the analysis of the step response. First, we use a change of integration variables to express the image as:

$$\begin{aligned} I\left(\vec{r}\right) &= \frac{1}{4}\int d^{2}q_{1}d^{2}q_{2}\,S\left(\frac{\vec{q}_{2}+\vec{q}_{1}}{2},\frac{\vec{q}_{2}-\vec{q}_{1}}{2}\right) \\ &\quad\times\hat{T}\left(\frac{\vec{q}_{2}+\vec{q}_{1}}{2}\right)\hat{T}\left(\frac{\vec{q}_{2}-\vec{q}_{1}}{2}\right)^{*}\exp\left(2\pi i\vec{q}_{1}\cdot\vec{r}\right), \end{aligned} \tag{9}$$

For a step object we have:

$$T\left(\vec{r}\right)=\theta\left(x\right), \tag{10}$$

with FT:

$$\hat{T}\left(\vec{q}\right)=\frac{\delta\left(q_{y}\right)}{2\pi i\left(q_{x}-i\varepsilon\right)}, \tag{11}$$

and ε an infinitesimal real positive number. Inserting this expression in the general formula for the intensity gives the Edge Spread Function $\mathrm{ESF}\left(x\right)\equiv I\left(x\right)$. The Line Spread Function then follows by differentiation as:

$$\mathrm{LSF}\left(x\right)\equiv\frac{dI\left(x\right)}{dx}=\int dq\hat{H}\left(q,0\right)\exp\left(2\pi iqx\right). \tag{12}$$

where $\hat{H}\left(q,0\right)$ is the apparent OTF extracted from the LSF, which is Hermitian ($\hat{H}\left(q,0\right)=\hat{H}\left(-q,0\right)^{*}$) because the LSF is real. This apparent OTF can thus be measured in a straightforward way by measuring the ESF, differentiation to obtain the LSF, and finally Fourier Transformation (see Fig. 1b), an approach we also follow in our experimental analysis. It is stressed that the quantity measured in this way, and the associated apparent PSF, are not in any sense a true OTF and PSF, because of the inherent non-linear nature of the image formation process in partially coherent imaging systems.

The apparent OTF can be related to the TCC by:

$$\hat{H}\left(q,0\right)=\frac{i}{\pi}\int_{-\infty}^{+\infty}dq'\,\frac{qS\left(\left(q'+q\right)/2,0,\left(q'-q\right)/2,0\right)}{q'^{2}-\left(q-i\varepsilon\right)^{2}}. \tag{13}$$

Using the Plemelj formula of complex analysis:

$$\frac{1}{q-i\varepsilon}=P\left(\frac{1}{q}\right)+i\pi\delta\left(q\right), \tag{14}$$

where 'P' indicates the principal value, it may be shown that:

$$\hat{H}(q,0) = \frac{1}{2}\left(\hat{Q}(q,0) + \hat{Q}(-q,0)^*\right) + \hat{U}(q,0), \tag{15}$$

with:

$$\hat{U}(q,0) = \frac{i}{\pi} P \int_{-\infty}^{+\infty} dq' \, \frac{qS\left(\left(q'+q\right)/2, 0, \left(q'-q\right)/2, 0\right)}{q'^2 - q^2}. \tag{16}$$

a Hermitian function of q ($\hat{U}(q,0) = \hat{U}(-q,0)^*$). Apparently, the first term on the right hand side of Eq. (15) can be directly related to the TCC and the performance function, but the second term on the right hand side of Eq. (15) is considerably more involved. The apparent OTF can be generalized from the x-oriented edge giving the apparent OTF at spatial frequency vectors $\vec{q} = (q,0)$ to an arbitrary edge orientation giving the apparent OTF at spatial frequency vectors $\vec{q} = (q_x, q_y)$ as:

$$\hat{H}(\vec{q}) = \frac{1}{2}\left(\hat{Q}(\vec{q}) + \hat{Q}(-\vec{q})^*\right) + \hat{U}(\vec{q}), \tag{17}$$

The edge response and the LSF derived from it depend on the edge type for partially coherent systems. Repeating the previous analysis for a general edge profile $T(x,y) = a - b/2 + b\theta(x)$ with a and b arbitrary complex numbers, gives a LSF:

$$\frac{dI(x)}{dx} = \mathrm{Re}\left\{2a^* b\, Q(x,0)\right\} + |b|^2 U(x,0), \tag{18}$$

where $U(\vec{r})$ is the inverse FT of $\hat{U}(\vec{q})$. The apparent OTF for an arbitrary edge orientation then follows as the linear combination:

$$\hat{H}(\vec{q}) = a^* b \hat{Q}(\vec{q}) + a b^* \hat{Q}(-\vec{q})^* + |b|^2 \hat{U}(\vec{q}). \tag{19}$$

The amplitude edge case, for which the Hermitian part of the performance function appears, is retrieved for $a = 1/2$ and $b = 1$. For a $\pi/2$ phase edge ($a = 1$, $b = 2i$) the ant-Hermitian (imaginary & antisymmetric) part of the performance function appears rather than the Hermitian part. For a π phase edge ($a = 0$, $b = 2i$) the performance function plays no role at all. In the weak object limit ($|a| \gg |b|$) the partially coherent system becomes linear and the LSF is fully determined by the performance function.

For the unaberrated case it appears that $\hat{Q}(\vec{q})$ is real and symmetric, and $\hat{U}(\vec{q})$ is imaginary and antisymmetric. It follows that the real symmetric part of the apparent OTF is determined by the FT of the performance function, and the imaginary antisymmetric part of the apparent OTF is determined by the transfer function $\hat{U}(\vec{q})$. An asymptotic analysis of Eq. (16) in the limit $\sigma \gg 1$ (see Appendix) results in an apparent Phase Transfer Function (PTF) equal to:

$$\arg\left\{\hat{H}(\vec{q})\right\} = -\frac{q\lambda}{\pi \mathrm{NA}\sigma}, \tag{20}$$

which implies that close to the incoherent limit the primary effect of partial coherence is an apparent shift of the edge over a distance $\Delta x = \lambda/\left(2\mathrm{NA}\pi^2\sigma\right)$

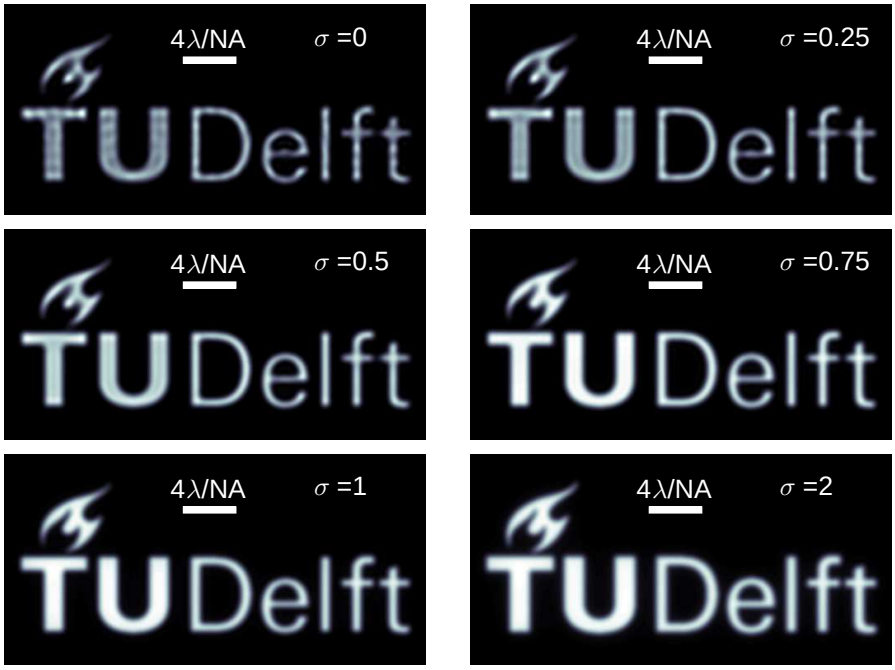

Figure 2: Simulated images of a phantom object for different values of the partial coherence factor.

towards the bright side of edge. This provides a quantitative description of the edge shifting effect first noted by Barakat [4]. It is noteworthy that this apparent edge shift persists for all finite σ, even though the real part of the OTF remains equal to the incoherent OTF for all $\sigma \geq 1$.

For the purpose of illustration simulated images of a phantom object for different values of σ are shown in Fig. 2, showing the effects of edge ringing and edge shift for the smaller values of σ.

2.2 Edge ringing

For the aberration-free case the FT of the performance function corresponds to the overlap integral of two displaced pupils, one with normalized radius equal to one, and the other with normalized radius equal to σ. An analytical expression for this overlap integral has been derived by Sheppard [19]:

$$\begin{aligned} \hat{Q}\left(\vec{q}\right) &= \frac{1}{\pi\sigma^2}\left[\arccos\left(\frac{\rho^2+1-\sigma^2}{2\rho}\right)\right. \\ &\left.+\sigma^2\arccos\left(\frac{\rho^2-1+\sigma^2}{2\sigma\rho}\right)-\sqrt{\rho^2-\left(\frac{\rho^2+1-\sigma^2}{2}\right)^2}\right], \end{aligned} \tag{21}$$

with the normalized spatial frequency $\rho = |\vec{q}|\,\lambda/\mathrm{NA}$, and where $1-\sigma \le \rho \le 1+\sigma$. For $\rho < 1-\sigma$ we have $\hat{Q}(\vec{q}) = 1$ and for $\rho > 1+\sigma$ we have $\hat{Q}(\vec{q}) = 0$, giving a spatial frequency cutoff equal to $(1+\sigma)\,\mathrm{NA}/\lambda$. Figure 3 shows the effective Modulation Transfer Function (MTF) $\left|\hat{Q}(\vec{q})\right|$ according to Eq. (21) for different σ values, showing the crossover from the fully coherent behavior at $\sigma = 0$ to the fully incoherent behavior at $\sigma = 1$. The performance function for the non-aberrated system appears to be the product of two Airy-distributions:

$$Q(\vec{r}) = \pi \left[\frac{2J_1(2\pi r \mathrm{NA}/\lambda)}{2\pi r \mathrm{NA}/\lambda}\right]\left[\frac{2J_1(2\pi r\sigma \mathrm{NA}/\lambda)}{2\pi r\sigma \mathrm{NA}/\lambda}\right]. \tag{22}$$

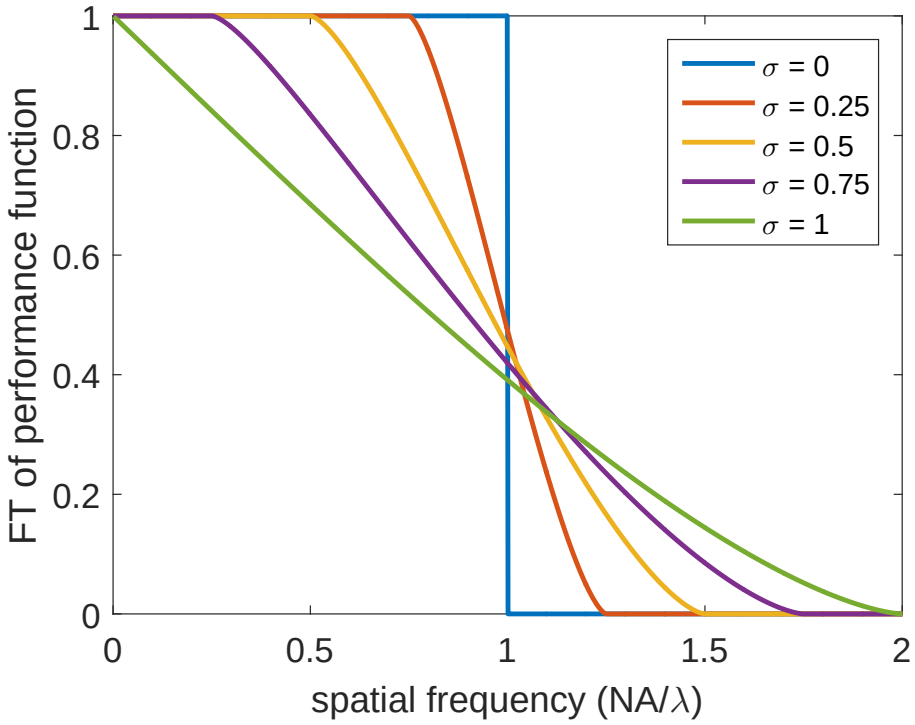

Figure 3: FT of the performance function, equal to the real part of the apparent OTF, as a function of spatial frequency of aberration-free in-focus partially coherent imaging systems for different values of the partial coherence factor σ.

Kintner and Stillitto [18] have derived a condition on the performance function that is necessary and sufficient for avoiding edge ringing. This condition is:

$$\mathrm{Re}\{Q(\vec{r})\} \ge 0 \tag{23}$$

for all positions $\vec{r}$. The performance function of Eq. (22) can become negative for any value $\sigma < 1$, thereby violating Kintner and Stillitto's condition. It may

be concluded that edge ringing can never be completely avoided in partially coherent imaging systems. The appearance of edge ringing may also be related to violations of the so-called Lukosz-bound [20]. We propose that a practical tolerance limit to avoid edge ringing may be derived by requiring that the first minimum of the first Airy distribution in Eq. (22) at $r = 0.817\lambda/\mathrm{NA}$ coincides with the first zero of the second Airy distribution in Eq. (22) at $r = 0.610\lambda/\sigma\mathrm{NA}$, implying that $\sigma = 0.610/0.817 \approx 0.75$. The rule-of-thumb is therefore that edge ringing will only become appreciable if σ drops below this critical value. The limit of $\sigma = 0.75$ corresponds to the actual practice in microscopy.

In digital imaging the edge ringing fringes in the measured step response are smoothed because the signal is integrated over the non-zero pixel size. We have performed a numerical simulation to assess this effect. First, the TCC is evaluated from Eq. (5) for a range of spatial frequencies $\vec{q}_1 = (q_{1x}, 0)$ and $\vec{q}_2 = (q_{2x}, 0)$ typically on a 257×257 grid of $q_{1x} \times q_{2x}$ values. Next, the 2D-FT of this array is computed using the chirp z-transform method [21] on a 1039×1039 grid of $x_1 \times x_2$ points, where the spacing of the grid points is 15 times smaller than the Nyquist sampling distance $\lambda/4\mathrm{NA}$. Then, the sum is taken over the matrix elements with $x_1 > x$ and $x_2 > x$ to obtain the ESF. A convolution over the pixel size $\lambda/4\mathrm{NA}$, in agreement with the Nyquist criterion, is done to take into account the finite pixel size. This convolution reduces the number of true data points to 1025, taking the discrete derivative gives the LSF in 1024 data points. Finally, applying a Tukey window, and again an FT using the chirp z-transform method gives the apparent OTF on a line of 257 spatial frequency points.

Figure 4a shows the numerically simulated edge response taking the smoothing effect into account, and Fig. 4b shows the corresponding edge overshoot values for different σ. We assume a pixel size $\lambda/4\mathrm{NA}$, in agreement with the Nyquist criterion. It is mentioned that the highest spatial frequency in the intensity signal $I(\vec{r})$ for an arbitrary 2D-object is $2\mathrm{NA}/\lambda$ for all σ, even though the highest spatial frequency of the complex amplitude object function $T(\vec{r})$ contributing to the intensity signal is $(1+\sigma)\,\mathrm{NA}/\lambda$. This justifies the use of the same Nyquist size pixels for all values of σ. It may be seen that the edge overshoot approaches zero when $\sigma \to 1$ and remains below 20% for all σ, for $\sigma = 0.75$ the edge overshoot is just 3.4%. Figure 4c shows the apparent MTF, and Fig. 4d shows the apparent PTF derived from the edge responses shown in Fig. 4a. The MTF-curves confirm that the signal contains spatial frequencies up to $2\mathrm{NA}/\lambda$, the non-zero PTF-curves result from the asymmetry in the LSF and approach the linear slope of Eq. (20) close to the incoherent limit. The increase in the apparent MTF for the lower spatial frequencies with decreasing σ agrees with the findings of Ref. [17] for the square aperture case. For $\sigma < 1$ the OTF is fully imaginary for spatial frequencies $q > (1+\sigma)\,\mathrm{NA}/\lambda$, giving a plateau equal to $-\pi/2$ in the PTF (up to numerical errors of a few degrees). Figure 4e and f show the numerically simulated real and imaginary part of the apparent OTF. The real part of the apparent OTF substantially agrees with the theoretical curves shown in Fig. 3, the non-zero imaginary part of the apparent OTF prove that the FT of the performance function is not identical to the apparent OTF

for an amplitude edge.

2.3 Depth Of Focus

The next important factor to investigate is the dependence on defocus. There are two complications in this analysis. The first is that the edge response and the attendant LSF depend on the object type and appear to depend on the FT of the performance function $\hat{Q}(\vec{q})$ for a weak edge, or generally on the transfer function $\hat{U}(\vec{q})$ as well. The second is that the sensitivity to defocus appears to depend on the spatial frequency.

We will first focus our attention on the transfer function $\hat{Q}(\vec{q})$ defined by the overlap integral Eq. (6) between a circle with unit radius and a circle with radius σ displaced over a distance $\rho = |\vec{q}|\,\lambda/\mathrm{NA}$. The aberration function for defocus in the paraxial limit of low NA is:

$$W(x,y) = \frac{1}{2} z \mathrm{NA}^2 \left(x^2 + y^2\right). \tag{24}$$

with z the defocus and $\vec{\rho} = (x,y)$ the normalized pupil coordinates. The phase in the overlap region of the two circles with unit radius and radius σ then is:

$$\begin{aligned} \Delta\Phi(\rho,x,y) &= \frac{2\pi}{\lambda}\left(W(x,y) - W(x-\rho,y)\right) \\ &= \frac{\pi z \mathrm{NA}^2}{\lambda}\left(2\rho x - \rho^2\right), \end{aligned} \tag{25}$$

which has a maximum value in the overlap region at $(x,y) = (1,0)$ and a minimum at $(x,y) = (\rho-\sigma, 0)$, giving a peak-valley value:

$$\begin{aligned} \Phi_{\mathrm{p-v}}(\rho) &= \Delta\Phi(\rho,1,0) - \Delta\Phi(\rho,\rho-\sigma,0) \\ &= \frac{2\pi z \mathrm{NA}^2 \rho\,(1+\sigma-\rho)}{\lambda}. \end{aligned} \tag{26}$$

A significant decay of the modulus $\left|\hat{Q}(\vec{q})\right|$ due to a defocus z may be typically found if the distribution of phases in Eq. (25) across the overlap region spans the range from 0 to $\beta\pi$, where β is a numerical factor on the order of unity. Requiring $\Phi_{\mathrm{p-v}}(q) = \beta\pi$ results in an 'in-focus' layer $\Delta z/2 \le z \le \Delta z/2$ for which $-\beta\pi \le \Phi_{\mathrm{p-v}}(q) \le \beta\pi$ with thickness:

$$\Delta z = \frac{\beta\lambda}{\mathrm{NA}^2 \rho\,(1+\sigma-\rho)}. \tag{27}$$

The minimum of this defocus range as a function of normalized spatial frequency ρ occurs at $\rho = (1+\sigma)/2$ and may be identified with the Depth Of Focus:

$$DOF = \frac{4\beta\lambda}{\mathrm{NA}^2\,(1+\sigma)^2}. \tag{28}$$

The numerical factor β takes different values depending on the degree of defocus which is tolerated. The analog to Maréchal's diffraction limit may be found by requiring a peak-valley phase in the overlap integral $\Phi_{\mathrm{p-v}}(q) = \pi$, which corresponds to the crossover point from constructive to destructive interference. This results in a value $\beta = 1/2$. Capturing the largest fraction of the 'in-focus' layer typically corresponds to $\beta = 2$, i.e. four times larger than the diffraction limit. It appears empirically that the Full Width Half Maximum (FWHM) of the through-focus transfer function $\left|\hat{Q}(\vec{q})\right|$ corresponds to $\beta \approx \sqrt{2}$. The use of a threshold on the through-focus MTF for defining a DOF metric has been proposed for incoherent imaging systems previously by Qiu et al. [22]. The scaling of Eq. (28) with σ as $1/(1+\sigma)^2$ has also been found by Ren et al. [15].

This analysis may be generalized to focusing into a medium with refractive index n and beyond the paraxial limit. The aberration function for defocus is then:

$$W(x,y) = nz\left(1 - \sqrt{1 - \mathrm{NA}^2\left(x^2+y^2\right)/n^2}\right), \tag{29}$$

where $\mathrm{NA} < n$ in order to restrict the discussion to propagating waves only (evanescent waves are explicitly ruled out). This results in a predicted allowable defocus range:

$$\begin{aligned} \Delta z &= \beta\lambda\left[\sqrt{n^2 - \mathrm{NA}^2(1-\rho)^2} + \sqrt{n^2 - \mathrm{NA}^2(\sigma-\rho)^2}\right. \\ &- \left.\sqrt{n^2 - \mathrm{NA}^2} - \sqrt{n^2 - \sigma^2\mathrm{NA}^2}\right]^{-1}. \end{aligned} \tag{30}$$

At normalized spatial frequency $\rho = (1+\sigma)/2$ we find the DOF as:

$$\begin{aligned} DOF &= \beta\lambda\left[2\sqrt{n^2 - \mathrm{NA}^2(1-\sigma)^2/4}\right. \\ &- \left.\sqrt{n^2 - \mathrm{NA}^2} - \sqrt{n^2 - \sigma^2\mathrm{NA}^2}\right]^{-1}. \end{aligned} \tag{31}$$

This analysis points to two salient features. First, the decay of the through-focus transfer function $\left|\hat{Q}(\vec{q})\right|$ as a function of defocus depends on the spatial frequency: For the middle spatial frequencies the decay is steep, for low and high spatial frequencies the decay is only mild. Second, for low σ the decay of the through-focus transfer function $\left|\hat{Q}(\vec{q})\right|$ with defocus is steeper than for high σ, implying that the DOF increases toward the coherent limit.

These predictions may be tested with a numerical computation of the through-focus transfer function $\left|\hat{Q}(\vec{q})\right|$ for different σ. Figure 5 shows these numerical results for a range of σ values. We have taken $\mathrm{NA} = 0.15$ so as be close to the paraxial limit. Figure 6 shows the FWHM-values as a function of spatial frequency numerically determined from the through-focus transfer function, and the model curves according to Eq. (27) with $\beta = \sqrt{2}$. The agreement between

the curves is very good for $\sigma \geq 0.5$ and describes the trend qualitatively for $\sigma < 0.5$.

As mentioned before, the transfer function $\hat{Q}(\vec{q})$ does not fully describe the LSF derived from the edge response. Figure 7 shows the apparent through-focus MTF $\left|\hat{H}(\vec{q})\right|$ derived from the amplitude edge response, and Fig. 8 shows the numerically determined FWHM-values as a function of spatial frequency. It appears that for spatial frequencies $q < \mathrm{NA}/\lambda$ the dependence of the FWHM on spatial frequency and partial coherence factor agrees reasonably well with the FWHM derived from the FT of the performance function. For larger spatial frequencies, typically above NA/λ, the FWHM drops to levels comparable to the FWHM for $\sigma = 1$ for all σ.

Focus errors in whole slide scanning occur for two reasons. First, the standard thickness of a tissue slide in pathology applications is 4 μm, which usually exceeds the DOF. Second, there are topography variations in the tissue layer across the total area of the tissue slide. Usually, an autofocus system is employed to let the objective lens follow these topography variations, but there may be residual focus errors, especially close to folds in the tissue layer where there is a steep rise in the topography. For these reasons it is advantageous to have a large DOF, because then focus errors have less impact on overall image quality. For example, it may be required that spatial details in the tissue structure down to about 2 μm remain clearly visible across a focus range equal to twice the tissue thickness of 4 μm (in order to be robust against topography variations and focus errors). Taking $\lambda = 0.56\mu$m, NA $= 0.75$ and $n = 1.5$ this corresponds to a spatial frequency of about $0.37\mathrm{NA}/\lambda$ and a defocus range of $\pm 2.99\lambda/2\left(n - \sqrt{n^2 - \mathrm{NA}^2}\right)$. From Eq. (30) it may then be inferred that the upper limit for σ should be in the range 0.65-0.70, somewhat smaller than typically used in microscopy.

2.4 Aberration estimation

Partial coherence also poses a challenge for extracting the primary aberrations from the through-focus apparent OTF derived from the step response, as proposed in our previous work [16]. In that work we described a method to measure coma from the maximum and minimum value of a third order polynomial fitted through the PTF. For σ values close to one or exceeding one it appears the apparent PTF in the aberration free case is more or less linear, pointing to an apparent shift in the edge position. It follows that this does not affect the estimation of coma. Figure 4 shows that for σ values considerably below one this is no longer the case.

Figure 9 shows the in-focus apparent PTF in case of 72 mλ root mean square (rms) coma for different values of the partial coherence factor σ and the coma estimated from these PTF-curves. The linear term in the PTF as a function of spatial frequency is calibrated by requiring the PTF to be zero at $q = \mathrm{NA}/2\lambda$, which determines the apparent edge shift. It appears that the procedure cannot be reliably used for $\sigma < 0.5$, as the PTF curve can then have

multiple local maxima/minima. For values $0.5 < \sigma < 1$ the procedure results in an underestimation of the true coma with errors up to a factor of 3. Clearly, depending on the value of σ the conversion factor between the coefficient of the third order polynomial that describes the PTF and the amount of coma must be adapted.

Spherical aberration deforms and bends the through-focus MTF pattern towards one focus side [16] resulting in a parabolic shape for the best focus line (which is defined as the maximum in the MTF as a function of defocus for each spatial frequency). The curvature of the best focus line appears to be a measure for spherical aberration [16]. Figure 10 shows a simulated through-focus apparent MTF in the presence of $72m\lambda$ rms spherical aberration. The best focus lines and the estimated spherical aberration according to the curvature of the best focus line for the different σ are plotted in Fig. 11. It can be seen that the curvature of the parabolic shape of the best focus curve decreases with decreasing σ, leading to an underestimation of the spherical aberration when the method of Ref. [16] is used. For small σ, typically for $\sigma < 0.5$, the best focus curve is even better approximated with a linear curve than a parabolic curve. So, similar to the case of coma, we may infer that the aberration estimation is unreliable for $\sigma < 0.5$ and the conversion factor between the parabolic curvature of the best focus line and the amount of spherical aberration must be adapted to the value of σ in the range $0.5 < \sigma < 1$.

3 Experiment

3.1 Scanner with compact flat-field Khler illumination unit

The experimental setup in use for whole slide imaging setup has been described in detail elsewhere [16]. Briefly, slides are imaged with a a Nikon 20X/NA0.75 Plan Apochromat objective lens and a double back-to-back achromat tube lens (two Thorlabs AC508-500-A, 500 mm focal length). The image data is captured using a Dalsa Piranha HS-40-04k40 TDI line scan sensor (4096 pixels, pixel size 7 μm$\times$7 μm, maximum frame rate 36 kHz) using pushbroom scanning. The apparent through-focus OTF is derived from the amplitude edge response of a custom-built resolution target that is imaged through-focus with 0.2 μm steps [16]. The resolution target consists of edges parallel and perpendicular to the scan direction. As the line sensor that scans the object is perpendicular to the scan direction the edges parallel to the scan direction are tangentially oriented w.r.t. the position in the Field Of View (FOV) of the objective lens and the edges perpendicular to the scan direction are sagittally oriented in the FOV of the objective lens. Both types of edges therefore give rise to an apparent OTF for two mutually perpendicular cross-sections of the pupil plane (the q_x and q_y directions). Both edges are measured for three positions in the FOV of the objective lens ($x \pm 0.5$ mm and $x = 0$ mm field position).

We have developed an illumination unit with the capacity to individually address the three primary colors red, green and blue. This can be used to

test chromatic aberration effects with a single camera and eventually to make color sequential scanning possible. Figure 12(a-b) show the realized illumination unit. It consists of three white LEDs selected from the Philips Luxeon Rebel series: cool white PWC1-0120, neutral white PWN1-0100, and warm white PWW1-0060 which are labeled as LED1, LED2, and LED3 respectively. Each LED has a 12 degree parabolic diffuse collimator (185-Polymer optics). A pair of dichroic filters from the Semrock catalog, FF495 (dichroic 1) and FF593 (dichroic 2), are used to divide the broad input light spectrum into the required red, green and blue bands. A photodiode sensor (PDA36A, Thorlabs), not drawn in Fig. 12b, monitors the light output of the LEDs. This photosensor is needed to guarantee a stable output with variable temperature and drift and to adjust relative intensities for maintaining color fidelity in a final RGB image generated with this illumination unit. Each LED is controlled by one general purpose laser diode driver (WLD-3343, Wavelength Electronics). It can modulate the LED current (maximum amplitude 3A) through an input voltage signal with a bandwidth limit of 2 MHz for a continuous sinusoidal signal, or 1 MHz for a square pulse train. A small mechanical mount for each LED-collimator assembly with 5 degrees of freedom alignment ($xyz\alpha\beta$) was constructed in order to align the beam profile of each LED at the entrance aperture of the condenser.

The collimated LED beams pass a circular top hat diffuser (ED1-C20, Thorlabs) with an engineered surface that provides a uniform angular distribution of the scattered light with a 20 degree scatter angle. As the top hat diffuser is placed at the back focal plane of the condenser this will result in a flat illumination field at the front focal plane with an inherent field stop with a diameter of 17 mm defined by the maximum scattering angle of the top-hat diffuser and the condenser focal length. The spectrum measured with an optical spectral analyzer (AQ-6315, Yokogawa) is shown in Fig. 12c. The three channels appear to cover and divide the entire visible spectrum in a reasonably acceptable way. The line profiles of the illumination beam at the targeted sample plane are shown in Fig. 12d-e. The illumination intensity across the imaged FOV (with diameter of about 1 mm) has good uniformity (variations typically below 10%) because of the top-hat diffuser.

The condenser is a triplet design of ordinary CVI-MellesGriot catalogue BK7 plano-spheres, one f=15mm/D=12.5mm lens and two f=37.5mm/D=25.0mm lenses, producing a condenser with NA = 0.75 and an overall focal length F = 10 mm. ZEMAX ray tracing simulations are shown in Fig.12f. This condenser design provides sufficient alignment margins and opportunities for creating a uniform intensity in the FOV and for providing Khler-illumination to a good degree. Placing an aperture stop at the entrance pupil allows for precise tuning of the partial coherence factor σ. The condenser NA for the complete set of apertures used was determined from a calibration measurement. For a set of apertures the condenser NA was measured by placing a pinhole at the focal plane of the condenser and a paper screen at a given distance d from the pinhole. The image of the projected circle on the screen is captured by a camera, which is used to calculate the radius a. The condenser NA then follows

as $\sin(\theta) = a/\sqrt{a^2 + d^2}$. For each aperture stop, the displayed NA data point is the average value of estimations for different distances d. The measurement result are shown in Fig.12g along with the corresponding NA values from a ZEMAX ray tracing simulation. The variation of the condenser NA with aperture stop radius R for an ideal condenser follows from the Abbe sine condition [3]. According to this condition the ratio of the off-axis object height (here the aperture radius R) to the sine of the angle of the rays in image space (here the condenser NA) must be constant to have the optical system free of aberrations (coma) to first order in the field coordinates. This ratio is the effective focal length of the condenser. This implies a linear relation NA $= R/F$, with R the aperture radius and F the condenser focal length. It appears that the estimated NA from the ray tracing simulation deviates from the aplanatic line, which possibly indicates inherent spherical aberration in the condenser design. The deviation in the measured NA is even a bit larger. This can possibly be due to misalignment induced spherical aberration in the experimentally realized condenser. The calibration data can be reasonably fitted with a straight line $0.077 + R/(13.0mm)$. This linear fit is subsequently used to assess the condenser NA for apertures used in the measurements of the through-focus apparent OTF. The aperture diameters equal to 4.0, 7.0, 8.5, 10,0, 11.5, 14.0, and 17.0 mm then result in partial coherence factors σ equal to 0.31, 0.46, 0.54, 0.62, 0.69, 0.82, 0.97, respectively.

3.2 Experimental results

A typical example of the measured edge response is shown in Fig.13, which shows measured intensity profiles at the center of the FOV of the objective lens for tangentially oriented edges. It appears that the edge overshoot is typically below 10% for all σ values tested, a bit lower than expected from the simulations. The edge overshoot does vary with edge orientation, FOV position, and color, occasionally giving rise to higher values for the edge overshoot.

Figure 14 and 15 show the measured apparent MTFs and PTFs at the best focus for different values of σ for both tangentially and sagittally oriented edges for three positions in the FOV. Overall we observe an increase in the apparent MTF with decreasing σ for spatial frequencies below NA$/\lambda$, in agreement with theoretical expectations, but the flat plateau for spatial frequencies below $(1 - \sigma)\,\mathrm{NA}/\lambda$ is in most cases not seen. The apparent PTF also increases in absolute value with decreasing σ, but only slightly. The apparent PTF is determined with the procedure outlined in Ref. [16], which effectively cancels the PTF term linear in spatial frequency (the apparent edge shift) described in the theory section. The residual PTF that depends non-linearly on spatial frequency appears to be somewhat smaller than expected from theory. It is noted that the overall edge response and edge overshoot, as well as the apparent MTF and PTF vary quite a bit with edge orientation and FOV position. This is indicative for field-dependent aberrations. Applying the estimation method of Ref. [16] to the PTF-data for $\sigma = 0.97$ results in rms tangential coma values that vary linearly with the field coordinate between $35 \pm 24\ m\lambda$ rms for the left

position in the FOV to $-53 \pm 24\ m\lambda$ for the right position in the FOV. Sagittal coma is largely independent of the field position and takes a rms value equal to $-5 \pm 13\ m\lambda$. The dependence of these aberrations on the field coordinate is in good agreement with so-called Nodal Aberration Theory (NAT) [23], which describes the impact of misalignment on the field dependence of the primary aberrations following from basic optical theory [3].

The overall through-focus apparent MTF data for tangentially and sagittally oriented edges is shown in Fig. 16 and Fig. 17, respectively. The overall shape fits reasonably well with the expectations from theory and simulation. Differences may be attributed to aberrations. For example, the mild curvature of the best focus lines for $\sigma = 0.97$ and the small asymmetry between the apparent MTF above and below best focus indicates the presence of spherical aberration. Averaging the spherical aberration estimates for all recorded through-focus edges in the resolution target gives an estimate of $49 \pm 17\ m\lambda$ rms spherical aberration. The difference between the best focus curves for tangentially and sagittally oriented edges is indicative for astigmatism. It appears that the astigmatism is below 10 mλ at the center of the FV and close to the diffraction limit at $\pm 0.5\ \mu$m in the FOV. This corresponds to a difference in best focus between sagittally and tangentially oriented edges of about 1.5 μm. The overall dependence of astigmatism (and field curvature) on the field coordinate is well described by a quadratic function, in agreement with basic optical theory [3, 23].

The sensitivity to defocus in the experiment is also analyzed. Figure 18 shows the FWHM of the apparent MTF as a function of spatial frequency for different σ. The FWHM increases with decreasing spatial frequency (in the range below NA/λ) and with decreasing partial coherence factor, roughly in agreement with the simulation data shown in Fig. 8. The FWHM data for σ close to one appears to follow the theoretical prediction of Eq. (30) rather well. This is reasonable as for higher values of σ the apparent MTF closely resembles the modulus of the FT of the performance function. The increase of the FWHM with decreasing σ, however, is steeper than the typical $1/\left(1+\sigma\right)^2$ factor derived for the axial width of the FT of the performance function. Close to the spatial frequency NA/λ the FWHM for all σ values reach the same minimum value of about $\lambda/\sqrt{2}/\left(1-\sqrt{1-\mathrm{NA}^2}\right)$.

4 Discussion

We have presented results concerning the effect of partial coherence on edge contrast, edge overshoot, and tolerance for defocus via a study of the through-focus apparent OTF derived from the response of the imaging system to amplitude edges. The analytical, numerical and experimental data agree reasonably well, where the deviations of the experiment from theory and simulation is attributed to aberrations.

There are several shortcomings to our experimental analysis. First of all, the measured edge response is somewhat undersampled, which makes the apparent OTF for the aliased higher spatial frequencies unreliable and which complicates

the quantitative assessment of edge overshoot. In future studies it may be advisable to implement the slanted edge approach in measuring the apparent OTF [24, 25]. The second aspect concerns the experimental assessment of the mutual intensity. Although the back aperture of the condenser is well filled and the condenser NA is determined from an experimental calibration, we have not actually measured the distribution of illumination light over the different illumination angles, let alone quantitatively measured the correlation between the light field at different positions in the illuminated FOV. So, the use of the mutual intensity following from Eq. (3) described by a single experimentally determined parameter σ may be too idealized.

Several factors have to be taken into account in order to determine the optimum value for σ for the application in WSI systems for digital pathology. A larger value of σ is beneficial for lateral resolution and edge ringing, whereas a smaller value of σ is beneficial for the edge contrast and DOF. It is questionable whether sufficient signal-to-noise ratio can be achieved for the very highest spatial frequencies in the range $(1.75 - 2)\,\mathrm{NA}/\lambda$, corresponding to spatial details in the range $(0.37 - 0.42)$ μm for $\lambda = 0.56$ μm and NA $= 0.75$. This implies that σ values above 0.75 hardly have an impact on the practical lateral resolution, even though the theoretical limit increases as $(1 + \sigma)\,\mathrm{NA}/\lambda$. On the other hand, the edge contrast, which is correlated to the transfer for lower spatial frequencies, typically up to NA/λ (spatial detail down to 0.75 μm), improves when σ is decreased to even lower values than 0.75 (see Fig. 14). The DOF also improves for this lower range of spatial frequencies. The DOF quantified by the FWHM of the through-focus apparent MTF (see Fig. 17) improves by 20 to 60%, depending on spatial frequency, when σ is lowered from 0.75 to 0.5. It appears that the FWHM of the apparent through-focus MTF is about equal to the typical tissue thickness of 4 μm for spatial details on the order of 2 μm when σ is decreased to about 0.5 for the set of imaging parameters used in the experiments. The major drawback of this further lowering of σ is the increase in edge ringing. The edge overshoot percentage used to quantify edge ringing is below 10% in simulation when $\sigma > 0.55$, and even a bit lower in the actual experiment. Taking all these factors into account it seems a reasonable assessment that the optimum value of the partial coherence factor σ is in the range 0.55-0.75. Although the research methods differ, this is substantially the same result as found by Ren et al. [15].

The current analysis has focused exclusively on circular apertures. An extension to different illumination apertures, in particular annular apertures and other variants of off-axis illumination, may have relevance to applications using such apertures. Starting point in that direction may be the work of Watanabe, who has analyzed the effects of partial coherence on DOF for an illumination system with one on-axis beam and two off-axis beams [26]. An entirely different generalization of the treatment described in this paper is towards other object types than edge objects. Point objects or periodic objects, for example, may lead to alternative approaches for measuring and monitoring optical image quality in the framework of a particular application. For any object $w(\vec{r})$ against a uniform background (object function $T(\vec{r}) = a + bw(\vec{r})$) the term in the image

signal linear in $w(\vec{r})$ is in fact the real part of the convolution of the object function and the performance function $\mathrm{Re}\{a^* bQ(\vec{r}) \otimes w(\vec{r})\}$. For a weak object ($|b| \ll |a|$) this convolution term contains all the relevant information on the object, making the performance function the weak object PSF and its FT the weak object OTF [19]. In that sense the FT of the performance function is the most relevant transfer function to assess the effects of partial coherence in general. An alternative may be found in the phase-space imaging kernel recently proposed in Ref. [27]. Finally, a comparison of our description of the effect of the finite degree of coherence on DOF to the theory of focusing of partially coherent waves with e.g. the Gaussian Schell-model [28, 29] may also offer new insights.

References

[1] H. H. Hopkins, "The concept of partial coherence in optics", Proc. Phys. Soc. London, Section A, **208**, 263–277 (1951).

[2] H. H. Hopkins, "On the diffraction theory of optical images", Proc. Phys. Soc. London, Section A, **217**, 408–432 (1953).

[3] M. Born and E. Wolf, *P*rinciples of Optics (Cambridge University, 1999).

[4] R. Barakat, "Partially coherent imagery in the presence of aberrations", Opt. Acta, **17**, 337–347 (1970).

[5] C. P. Kirk, "Aberration effects in an optical measuring microscope", Appl. Opt., **26**, 3417–3424 (1987).

[6] Y. Ichioka and T. Suzuki, "Image of a periodic complex object in an optical system under partially coherent illumination", J. Opt. Soc. Am., **6**, 921–932 (1976).

[7] R. Hild, G. Nitzsche, S. Kessler, and L. Leine, "Partially coherent defocused imaging of bar and periodic objects", Opt. Acta, **34**, 555–567 (1987).

[8] C. A. Mack, *F*undamental Principles of Optical Lithography: The Science of Microfabrication (Wiley, 2011).

[9] W. Singer, M. Totzeck, H. Gross, *H*andbook of Optical Systems, Physical Image Formation, Vol. 2 (Wiley, 2006).

[10] C. A. Mack, "Understanding focus effects in submicrometer optical lithography: a review", Opt. Eng., **32**, 2350–2362 (1993).

[11] M. op de Beeck et al., "NA/sigma optimisation strategies for an advanced DUV stepper applied to 0.25 μm and sub-0.25 μm critical levels", Proc. SPIE **3051**, 320–332 (1997).

[12] C. A. Mack, "Focus Effects in Submicron Optical Lithography, Part 4: Metrics for Depth of Focus"', Proc. SPIE **2440**, 458–471 (1995).

[13] M. von Waldkirch, P. Lukowicz, and G. Troster, "Effect of light coherence on depth of focus in head-mounted retinal projection displays", Opt. Eng., **43**, 1552–1560 (2004).

[14] M. von Waldkirch, P. Lukowicz, and G. Troster, "Multiple imaging technique for extending depth of focus in retinal displays", Opt. Express, **12**, 6350–6365 (2004).

[15] L. Ren, Z. Lia, Y. Li, B. Zheng, S. Li., X. Chen, and H. Liu, "The impact of the condenser on cytogenetic image quality in digital microscope system", Analytical Cellular Pathology, **36** 45–59 (2013).

[16] S. M. Shakeri, B. Hulsken, L. J. van Vliet, and S. Stallinga, "Optical quality assessment of whole slide imaging systems for digital pathology", Opt. Express, **23**, 1319–1336 (2015).

[17] M. N. Wernick and G. M. Morris, "Effect of spatial coherence on knife-edge measurements of detector modulation transfer function", Appl. Opt., **33**, 5906–5913 (1994).

[18] E. C. Kintner and R. M. Sillitto, "Edge-ringing in partially coherent imaging", Opt. Acta, **24**, 591–605 (1977).

[19] C. J. R. Sheppard, "Defocused transfer function for a partially coherent microscope and application to phase retrieval", J. Opt. Soc. Am. A, **21**, 828–831 (2004).

[20] C. H. Righolt et al., "Image filtering in structured illumination microscopy using the Lukosz bound", Opt. Express, **21**, 24431–24451 (2013).

[21] J. L. Bakx, "Efficient computation of optical disk readout by use of the chirp z transform", Appl. Opt., **41**4897–4903 (2002)

[22] Y. Qiu, X. Chen, Y. Li, B. Zheng, S. Li, W. R. Chen, and H. Liu, "Impact of the optical depth of field on cytogenetic image quality", J. Biomed. Opt., **17**, 096017 (2012).

[23] S. M. Shakeri, B. Hulsken, L. J. van Vliet, and S. Stallinga, "Shack-Hartmann sensor based optical quality testing of whole slide imaging systems for digital pathology", Proc. SPIE **9315** (2015).

[24] S. E. Reichenbach, S. K. Park, and R. Narayanswamy, "Characterizing digital image acquisition devices", Opt. Eng., **30**, 170–177 (1991).

[25] K. Masaoka, T. Yamashita, Y. Nishida, and M. Sugawara, "Modified slanted-edge method and multidirectional modulation transfer function estimation", Opt. Express, **22**, 6040–6046 (2014).

[26] H. Watanabe, "Analytical description of partially coherence optical systems for optimization of numerical aperture and degree of coherence", Jpn. J. Appl. Phys. **33**, 6549–6556 (1994).

[27] S. B. Mehta, and C. J. R. Sheppard, "Equivalent of the point spread function for partially coherent imaging", Optica **2**, 736–739 (2015).

[28] J. Pu, S. Nemoto, H. Zhang, W. Zhang, and W. Zhang, "Axial intensity distribution of partially coherent light focused by a lens with spherical aberration", J. Mod. Opt., **47**, 605–612 (2000).

[29] D. G. Fischer, and T. D. Visser, "Spatial correlation properties of focused partially coherent light", J. Opt. Soc. Am. A, **21**, 2097–2102 (2004).

4.1 Appendix

Here we present the asymptotic analysis for the imaginary part of the aberration free OTF for $\sigma \gg 1$. The TCC may generally be written as:

$$S\left(\frac{\vec{q}' + \vec{q}}{2}, \frac{\vec{q}' - \vec{q}}{2}\right) = \int d^2q''\, \hat{J}\left(\vec{q}'' - \frac{\vec{q}'}{2}\right) \hat{P}\left(\vec{q}'' + \frac{\vec{q}}{2}\right) \hat{P}\left(\vec{q}'' - \frac{\vec{q}}{2}\right)^* \tag{32}$$

Substituting in the expression for the transfer function $\hat{U}(q,0)$ Eq. (16) gives:

$$\hat{U}(q,0) = \frac{i}{\pi a^2} \int d^2q''\, R(\vec{q}'', q')\, \hat{P}\left(\vec{q}'' + \frac{q}{2}\hat{e}_x\right) \hat{P}\left(\vec{q}'' - \frac{q}{2}\hat{e}_x\right)^*, \tag{33}$$

with the weighting factor:

$$R(\vec{q}'', q') = a^2\, P \int_{-\infty}^{+\infty} dq'\, \frac{q\hat{J}\left(\vec{q}'' - \frac{q'}{2}\hat{e}_x\right)}{q'^2 - q^2}, \tag{34}$$

where $a = \min(\sigma, 1)$. With $\vec{q}'' = (q_x, q_y)$ and Eq. (3) we find that:

$$\begin{aligned} R(\vec{q}'', q') &= \frac{1}{\pi} P \int_{2q_x - 2\sqrt{\tau^2 - {q_y}^2}}^{2q_x + 2\sqrt{\tau^2 - {q_y}^2}} dq'\, \frac{q}{q'^2 - q^2} \\ &= \frac{1}{2\pi} P \int_{2q_x - 2\sqrt{\tau^2 - {q_y}^2}}^{2q_x + 2\sqrt{\tau^2 - {q_y}^2}} dq' \left[\frac{1}{q' - q} - \frac{1}{q' + q}\right], \end{aligned} \tag{35}$$

where $\tau = \sigma \mathrm{NA}/\lambda$. We may now use that:

$$P \int_a^b dx\, \frac{1}{x} = \log\left|\frac{b}{a}\right|, \tag{36}$$

to find:

$$\begin{aligned} R\left(\vec{q}'', q'\right) &= \frac{1}{2\pi}\left[\log\left|\frac{q_x + \sqrt{\tau^2 - {q_y}^2} - q/2}{q_x - \sqrt{\tau^2 - {q_y}^2} - q/2}\right|\right. \\ &\quad \left. - \log\left|\frac{q_x + \sqrt{\tau^2 - {q_y}^2} + q/2}{q_x - \sqrt{\tau^2 - {q_y}^2} + q/2}\right|\right] \\ &= \frac{1}{2\pi}\log\left|\frac{{q_x}^2 + {q_y}^2 - \tau^2 - q^2/4 + q\sqrt{\tau^2 - {q_y}^2}}{{q_x}^2 + {q_y}^2 - \tau^2 - q^2/4 - q\sqrt{\tau^2 - {q_y}^2}}\right|, \end{aligned} \tag{37}$$

For $\sigma \gg 1$ we may approximate this factor as:

$$R\left(\vec{q}'', q'\right) \approx \frac{1}{2\pi}\log\left|\frac{\tau - q}{\tau + q}\right| \approx -\frac{q}{\pi\tau}. \tag{38}$$

It then follows that:

$$\mathrm{Im}\left\{\hat{H}\left(q, 0\right)\right\} \approx -\frac{q}{\pi\tau}\mathrm{Re}\left\{\hat{H}\left(q, 0\right)\right\}, \tag{39}$$

giving as final result Eq. (20).

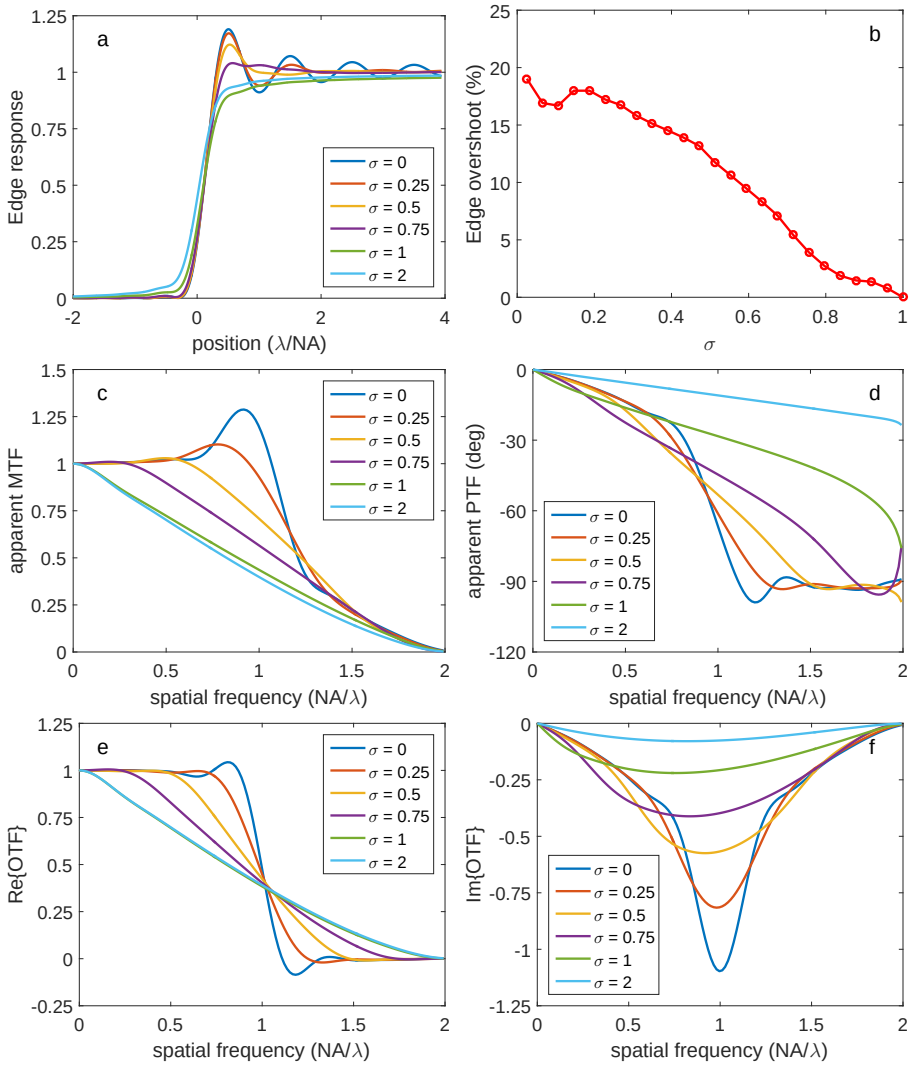

Figure 4: (a) Numerically computed edge response for different values of the partial coherence factor σ. (b) Edge overshoot as a function of the partial coherence factor σ. (c-d) Apparent MTF and PTF derived from the edge response for different values of the partial coherence factor σ. (e-f) Real and imaginary part of the apparent OTF derived from the edge response for different values of the partial coherence factor σ.

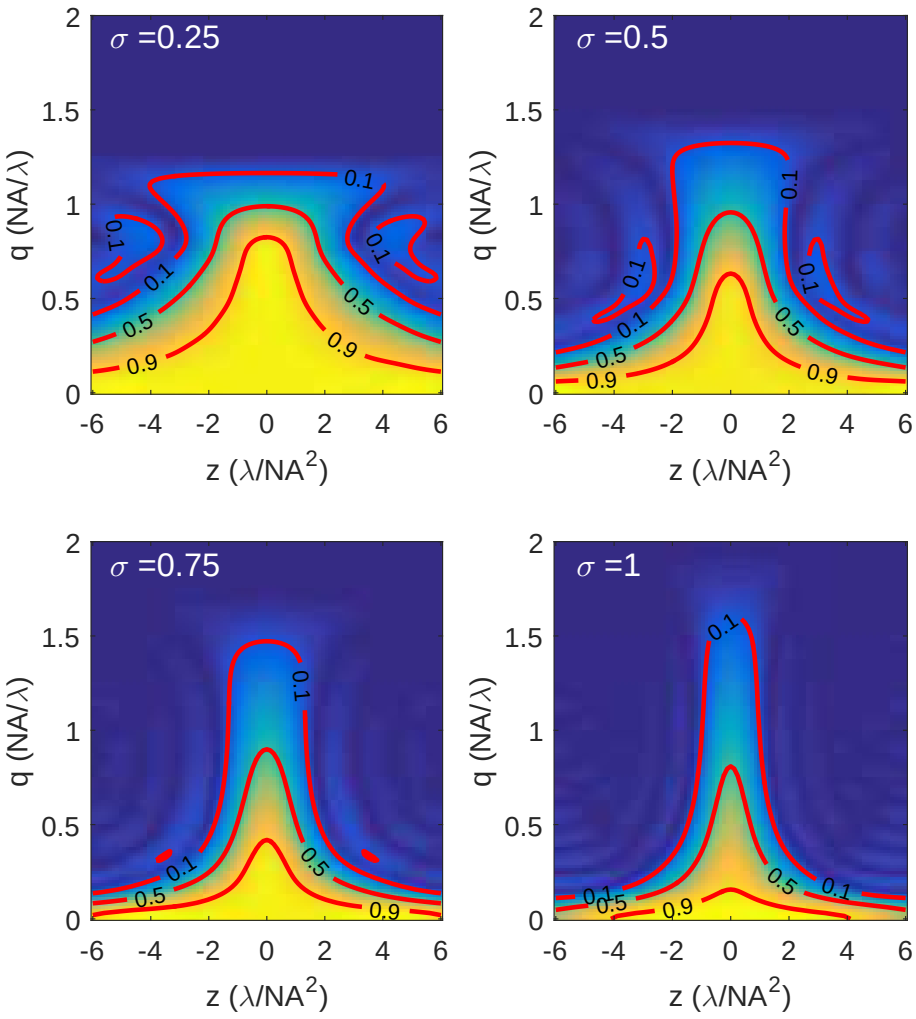

Figure 5: Numerically computed absolute value of the FT of the through-focus transfer function $\left|\hat{Q}\left(\vec{q}\right)\right|$ for different values of the partial coherence factor σ.

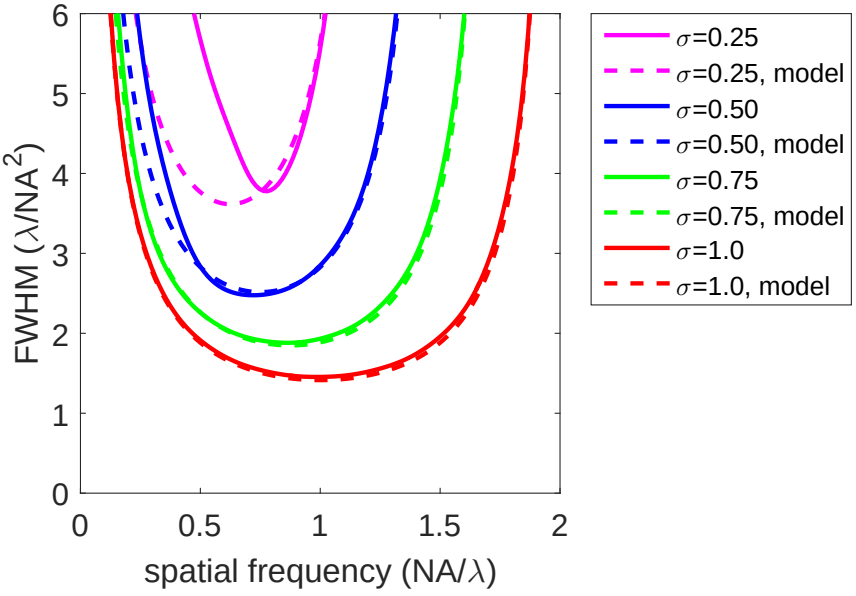

Figure 6: Numerically computed FWHM of the through-focus transfer function $\left|\hat{Q}\left(\vec{q}\right)\right|$ as a function of the spatial frequency for different values of the partial coherence factor σ and the corresponding predictions of Eq. (27) with $\beta = \sqrt{2}$.

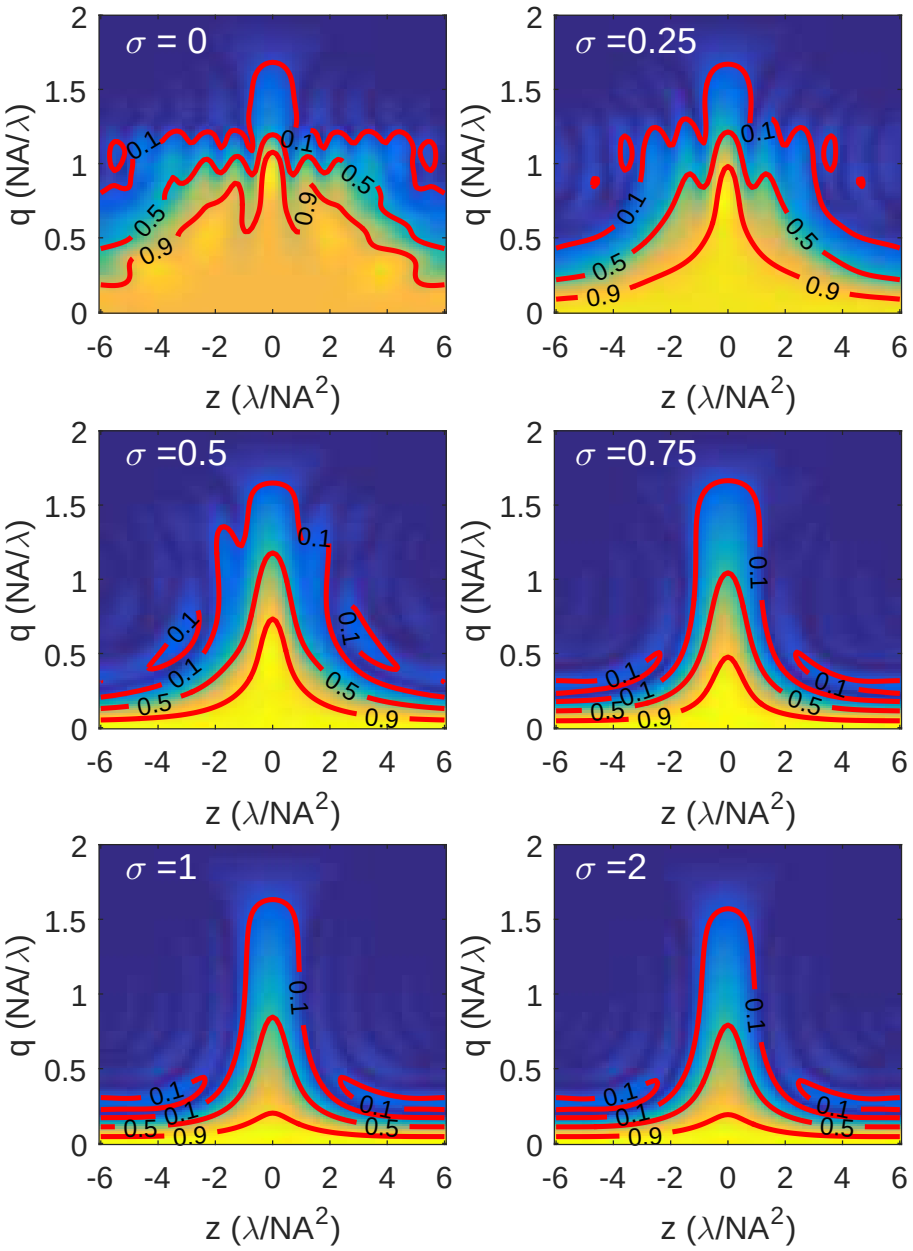

Figure 7: Numerically computed absolute value of the FT of the amplitude edge derived apparent MTF $\left|\hat{H}\left(\vec{q}\right)\right|$ for different values of the partial coherence factor σ.

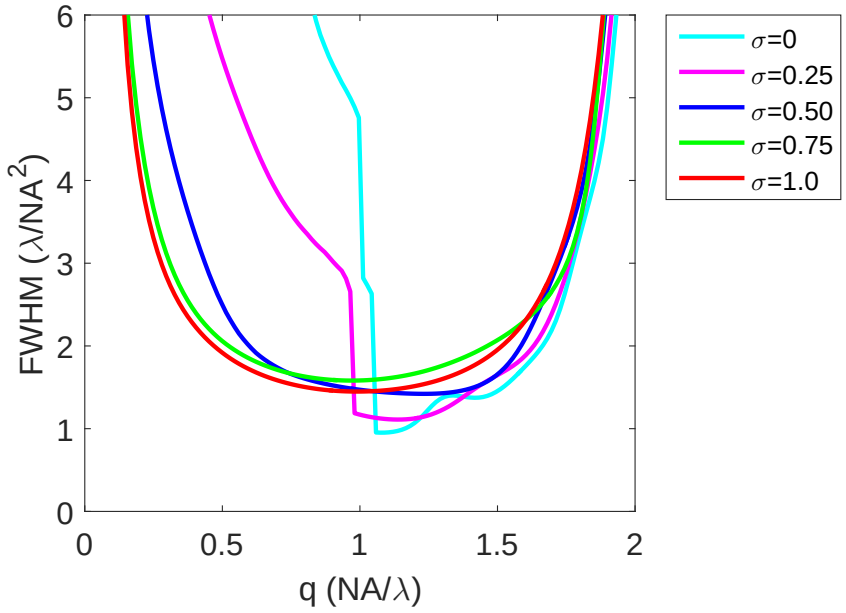

Figure 8: Numerically computed FWHM of the through-focus apparent transfer function derived from an amplitude edge $\left|\hat{H}\left(\vec{q}\right)\right|$ as a function of the spatial frequency for different values of the partial coherence factor σ.

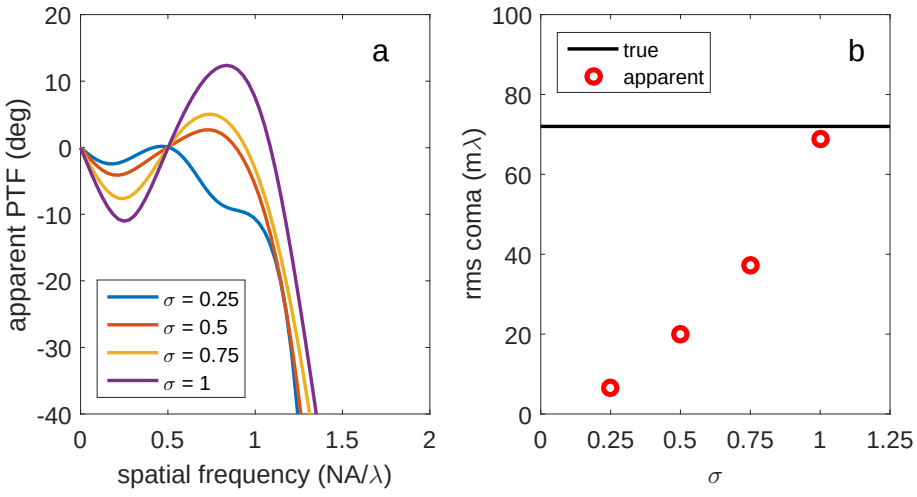

Figure 9: (a) Simulated PTF with 72 mλ rms coma for different values of the partial coherence factor σ values as a function of the spatial frequency. (b) The estimated coma based on the method of Ref. [16] as a function of σ.

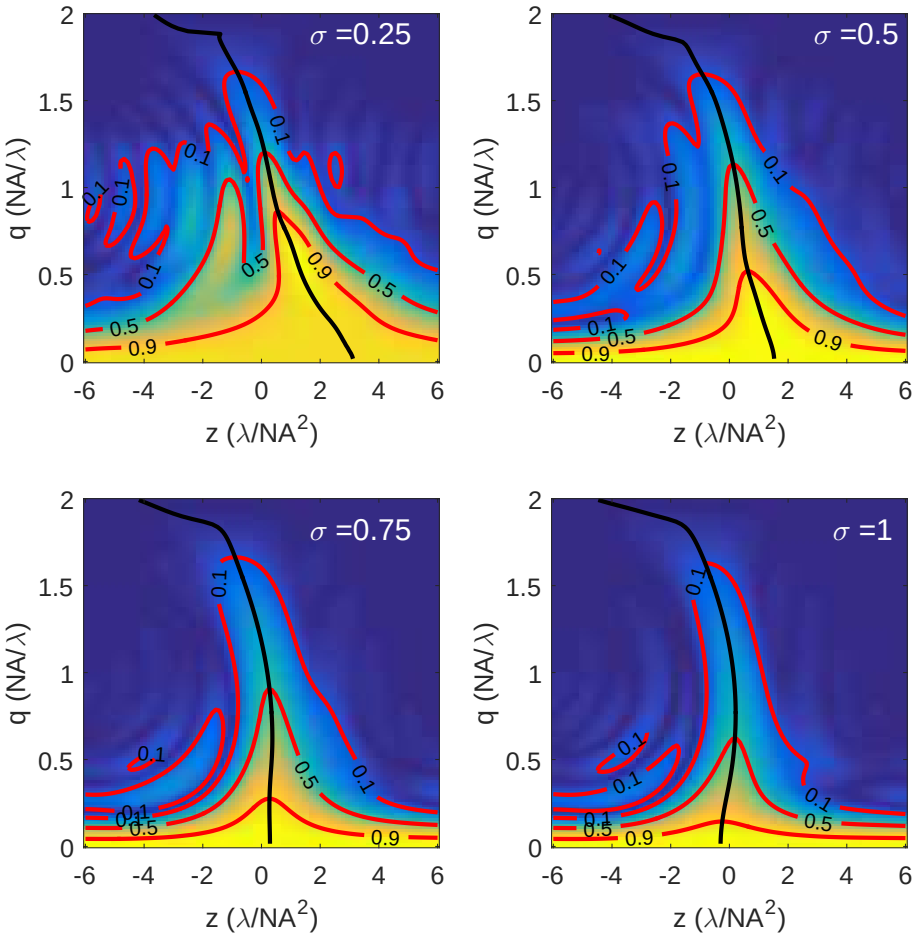

Figure 10: Simulated through-focus apparent MTF for $72m\lambda$ rms spherical aberration and the best focus curves for different values of the partial coherence factor σ.

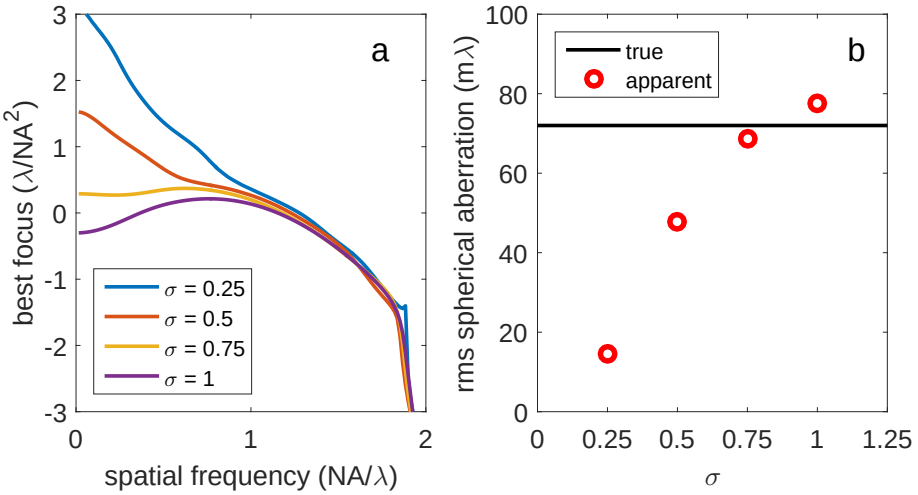

Figure 11: (a) Best focus as a function of spatial frequency for $72m\lambda$ rms spherical aberration. (b) Apparent spherical aberration estimated from the curvature of the best focus lines in (a).

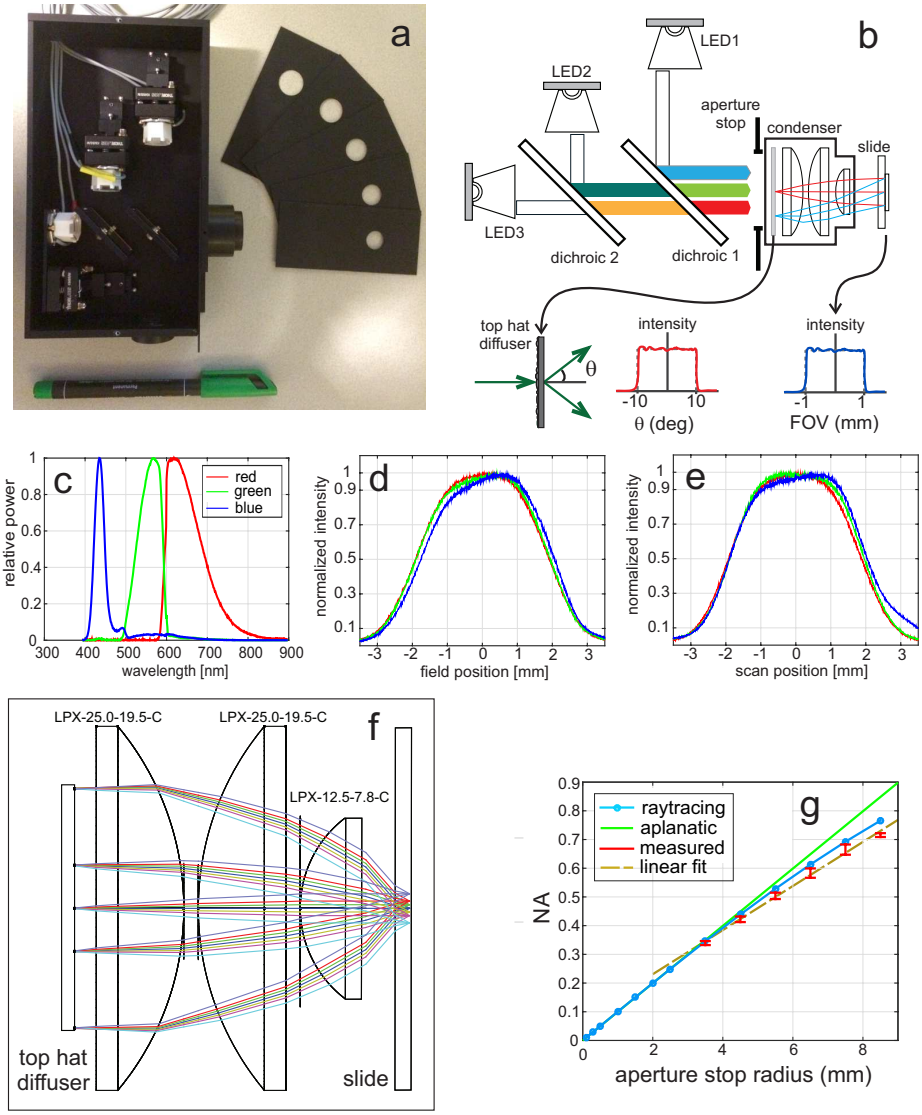

Figure 12: (a) Photo of the realized illumination unit with variable aperture stop size. (b) Schematic layout of the three-color LED-based illumination unit. The top hat diffuser scatters incident light uniformly within the angular range of (-10 deg, 10 deg). This results in a flat and spatially confined light distribution across the FOV. (c) Measured illumination box output light spectrum for red, green and blue color channels. (d-e) Measured condenser light profile along the field and scan direction, showing less than typically 10% intensity variation across the 1 mm diameter FOV. (f) Ray tracing picture of the triplet condenser design, rays are color coded for position in the FOV. (g) Condenser NA as a function of aperture stop radius, showing small deviations from aplanaticity.

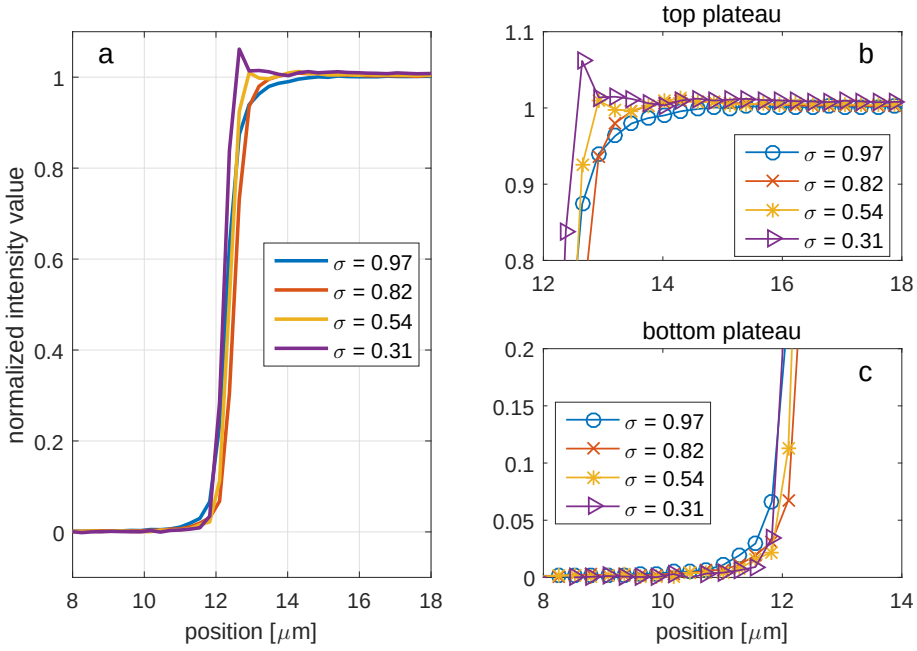

Figure 13: (a) Measured edge responses at the center of the FOV for tangentially oriented edges for different values of the partial coherence factor σ. (b-c) Insets of the top and bottom plateau, showing edge ringing for smaller σ.

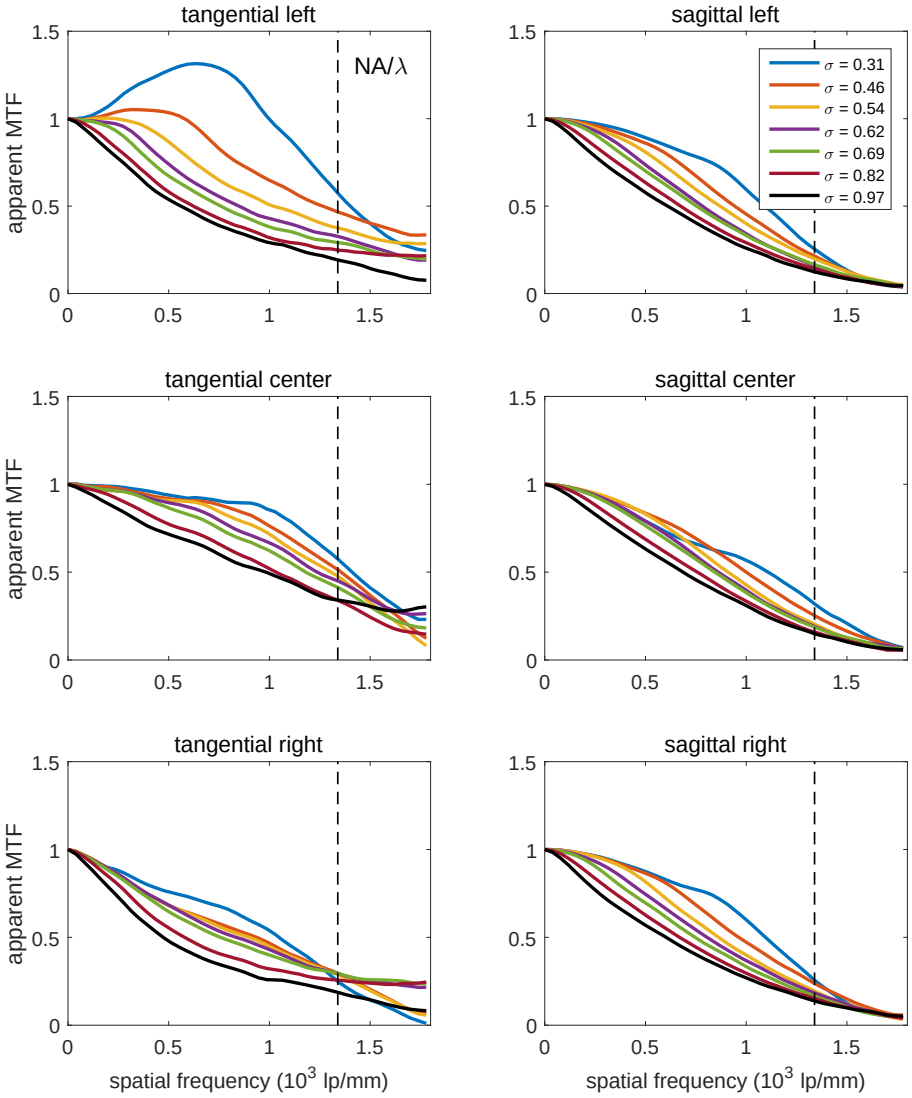

Figure 14: Measured in-focus apparent MTF curves for the green channel and for tangentially and sagittally oriented edges for the left (-0.5 mm), center and right (+0.5 mm) of the FOV for different values of the partial coherence factor σ. The dashed lines indicates the spatial frequency NA/λ.

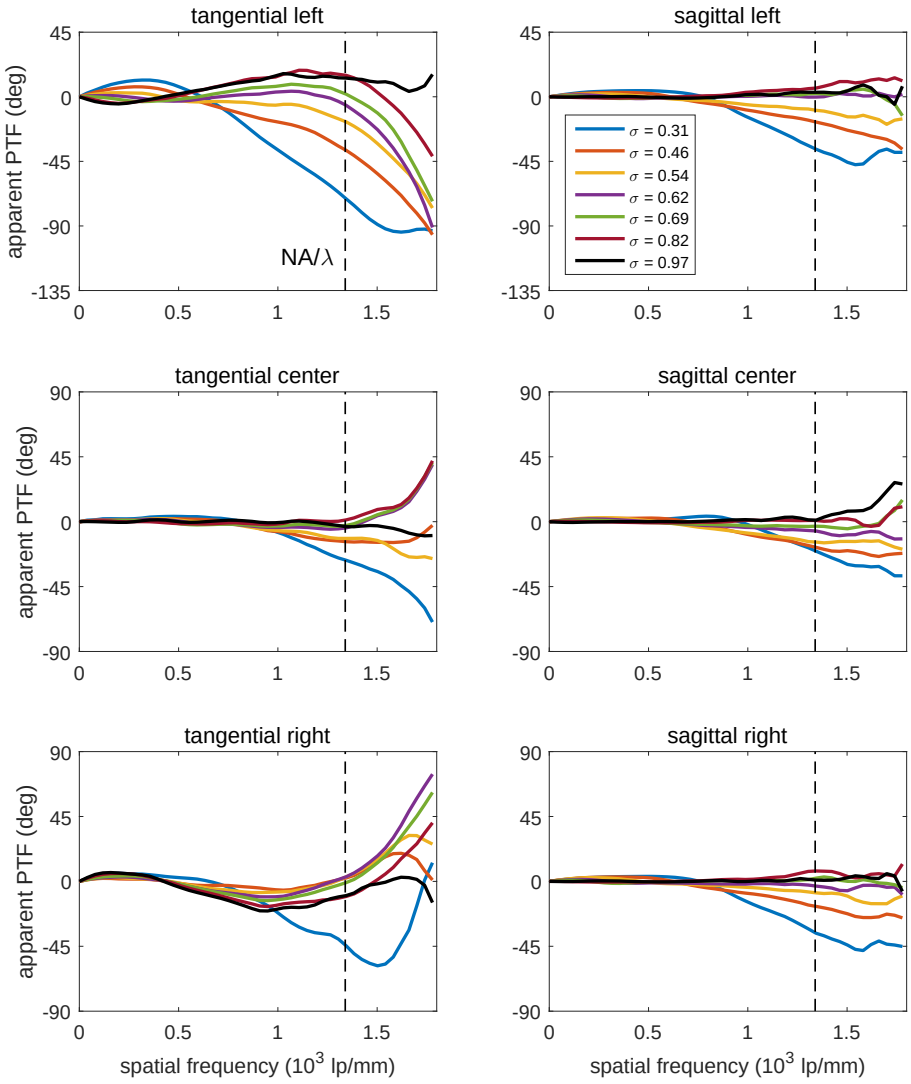

Figure 15: Measured in-focus apparent PTF curves for the green channel and for tangentially and sagittally oriented edges for the left (-0.5 mm), center and right (+0.5 mm) of the FOV for different values of the partial coherence factor σ. The dashed lines indicates the spatial frequency NA/λ.

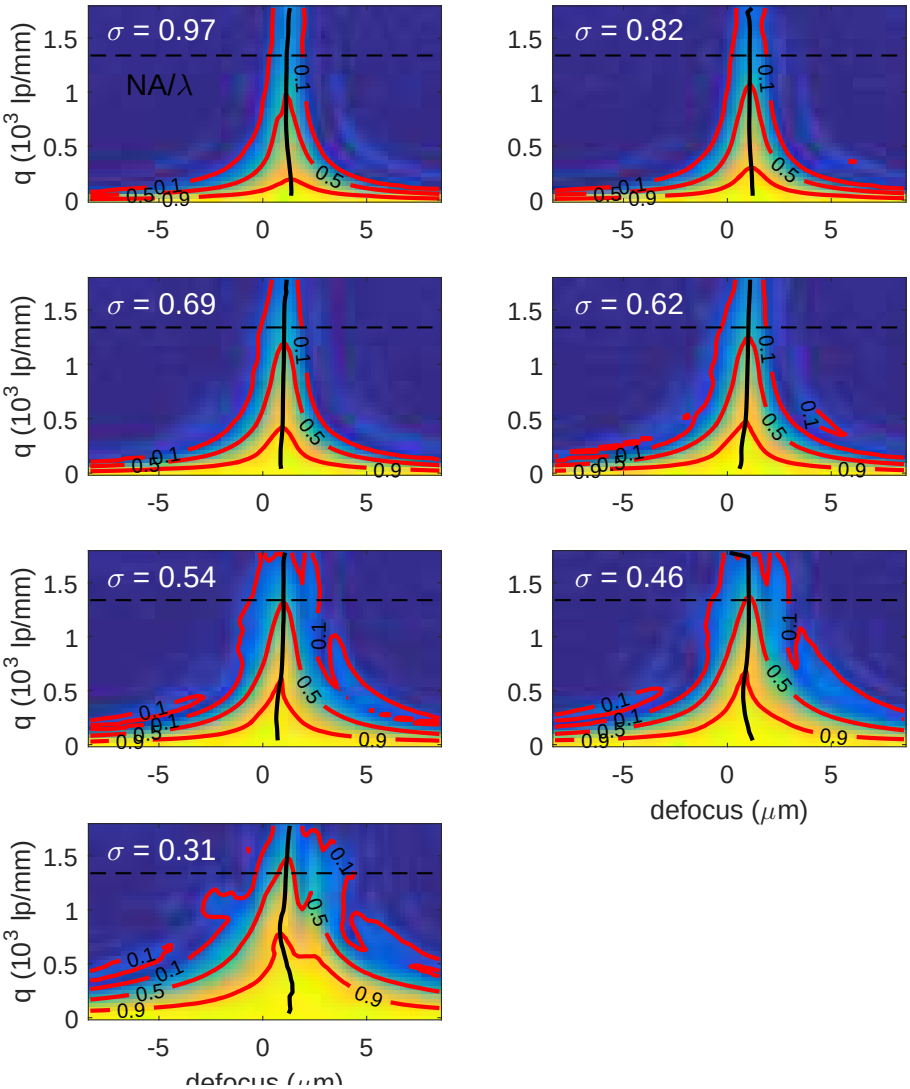

Figure 16: Measured through-focus apparent MTF curves for the green channel and for tangentially oriented edges in the center of the FOV for different values of the partial coherence factor σ. The dashed lines indicates the spatial frequency NA/λ.

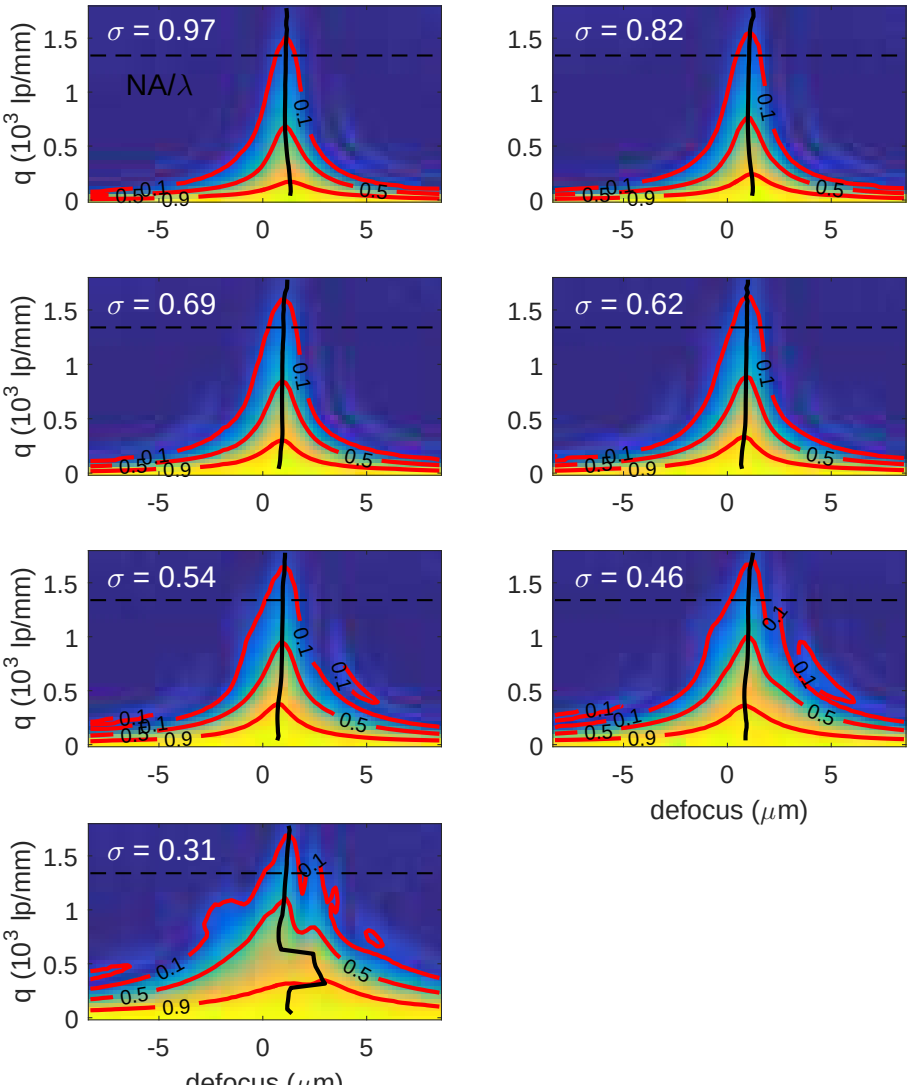

Figure 17: Measured through-focus apparent MTF curves for the green channel and for sagittally oriented edges in the center of the FOV for different values of the partial coherence factor σ. The dashed lines indicates the spatial frequency NA/λ.

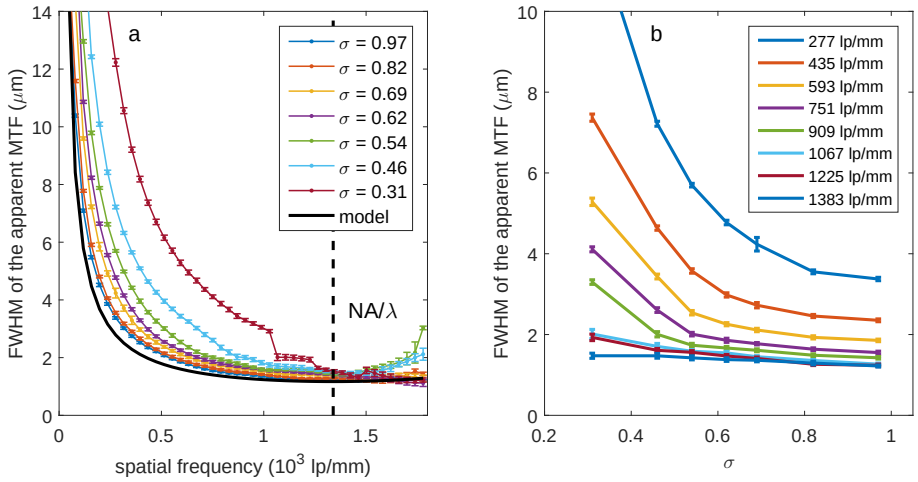

Figure 18: (a) FWHM of the apparent MTF (center of the FOV, green color channel) as a function of spatial frequency for different values of the partial coherence factor σ. The model curve is Eq. (30) for $\beta = \sqrt{2}$. (b) FWHM of the apparent MTF as a function of the partial coherence factor for different spatial frequencies.